AIP Advances

Method for reconstruction of axisymmetric capillary wave surface topography using inverse ray-tracing of refracted laser sheet

Cite as: AIP Advances **12**, 105322 (2022); https://doi.org/10.1063/5.0107154
Submitted: 02 July 2022 • Accepted: 24 September 2022 • Published Online: 28 October 2022

V. V. Mukim, R. W. Time, U. R. Kanade, et al.

Method for reconstruction of axisymmetric capillary wave surface topography using inverse ray-tracing of refracted laser sheet

Cite as: AIP Advances 12, 105322 (2022); doi: 10.1063/5.0107154
Submitted: 2 July 2022 • Accepted: 24 September 2022 •
Published Online: 28 October 2022

V. V. Mukim,[1,a] R. W. Time,[1] U. R. Kanade,[2] and A. H. Rabenjafimanantsoa[1]

AFFILIATIONS

[1] Department of Energy and Petroleum Engineering, University of Stavanger, Kjell Arholms Gate 41, 4021 Stavanger, Norway
[2] Oneirix Labs, Plot No. 6, Neelkamal Soc., Karvenagar, Pune 411052, India

[a] Author to whom correspondence should be addressed: vineet.v.mukim@uis.no

ABSTRACT

Capillary waves can be used to measure the fundamental fluid properties such as surface tension as well as, potentially, the viscosity of Newtonian fluids. This requires the measurement of various wave parameters, mainly wavelength, amplitude, and decay coefficient. However, the different scales of magnitudes make it a challenging task. Optical methods are well suited to analyze such problems due to their non-intrusive nature and high dynamic measurement resolution in both space and time. These methods are further categorized as point methods for a single probe measurement and space–time methods for transient measurement of the complete surface. Dynamic space–time methods are preferred despite the associated complex post-processing since they enable reconstruction of the wave surface. Some existing methods are discussed, and an improved method is then proposed to actually solve the associated inverse optics problem. In the method, an axisymmetric wave surface is re-constructed by analyzing the refracted laser sheet. The assumptions, simplifications, and constraints are taken to be compatible with experimental aspects for future validation. It is derived using the fundamental concepts in physics and the only major assumption of the axisymmetric nature of wave surface. The method exploits the underlying symmetry in the topography, making it more versatile, and suited for linear and non-linear capillary waves and waves with planar wavefront. The impact of parameters on the final result is determined through numerical simulations. Very low error (average and maximum) values are observed between reference and reconstructed topography for damped and undamped wave surfaces with a wide range of curvatures. Optimum values of critical parameters and associated reasoning are presented.

I. INTRODUCTION

A wave is defined as a disturbance traveling through a medium. For fluid media, waves can propagate both in single- and multiphase flows or at distinct interfaces. Waves that occur on the liquid–air interface are, thus, known as surface waves. Based on the dominant force, liquid surface waves are broadly categorized as

- gravity wave,
- capillary-gravity wave, and
- capillary wave.

Since such waves are mostly nonlinear and dispersive, there is also an interplay, reorganization, and energy transfer between the various wavelengths, e.g., for wind generated ocean waves (Munk[1]).

In Fig. 1, the vertical axis represents the relative amplitudes of ocean wind generated waves. In the highest frequency range of capillary waves associated with wavelengths in the (sub) millimeter range, there exist equations for the estimation of surface tension and viscosity of a Newtonian fluid (Behroozi[2]). These equations relate the fluid properties to wavelength and amplitude attenuation. They are derived from Navier–Stokes equations by Lighthill[3] and from the law of conservation of energy by Behroozi and Podolefsky.[4] Thus, the measurement of wavelength and amplitude becomes highly important for the study of capillary waves and their applications.

A classification of wave types along with various methods of generation and detection of waves is given by Slavchov *et al.*[5] The methods for measurement of waves are broadly classified as "point" methods or as "space–time" methods. Various excitation methods

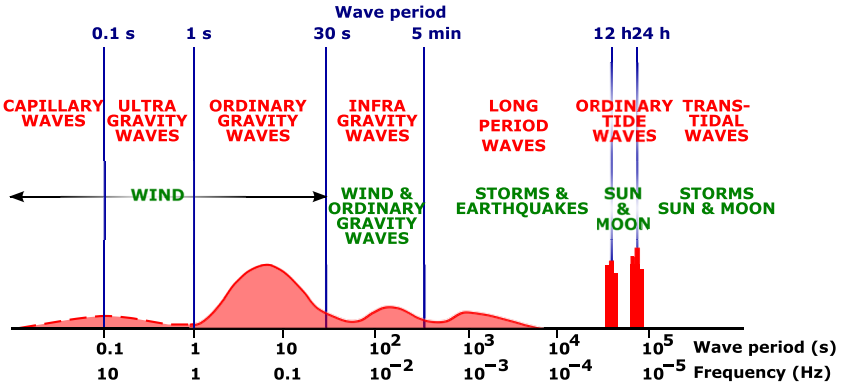

FIG. 1. Ocean wave classification according to wave amplitude and wave period. [Reproduced with minor changes in the axis labels from W. Munk, "Origin and generation of waves," in Proceedings of 1st International Conference on Coastal Engineering (1950), pp. 1–4. Copyright 1950 Author(s), licensed under a Creative Commons Attribution (CC BY) license.]

can be used to generate moving and standing waves. Then, the measurement of wavelengths and amplitudes are measured either locally ("point/spot" based) or as a full reconstruction ("space–time") of the whole wave surface in a given domain. The space–time methods provide more data about the wave surface but also require more post-processing. Optical measurement techniques are well suited for space–time methods in view of the relatively large amount of data required. Other advantages of optical techniques are their non-intrusive nature, their high resolution, and that they can be adapted both via wave and geometric optics. However, optical techniques are often associated with highly sensitive and sometimes expensive experimental setups. Utmost care, prior training, and experience are needed to use and operate systems that involve high powered lasers.

Some of the commonly used optical point measurement methods involve reflection, refraction, diffraction, and interference. A laser beam is often used as a monochromatic and coherent source of light. Neighboring consecutive peaks of the wave surface act as "diffraction grating" and the resulting Fraunhofer diffraction from the reflected light is used to obtain the wavelength of the wave surface. This is reported by Barik *et al.*,[6,7] Zhu *et al.*,[8] Nikolić and Nešić,[9] and Chowdhuri *et al.*[10] This method cannot be used to measure wave amplitude since the "diffraction grating" density is given by the wavelength and not much influenced by the amplitude. Saylor[11] used the principle of total internal reflection, whereas Palm *et al.*[12] and Saylor and Handler[13] used the shift in the single refracted beam of laser to measure the surface gradient. Behroozi[2,14,15] used interference of a reference beam and another beam reflecting from the wave surface in a single mode optic fiber to capture the amplitude. A little more flexibility was added with a moving probe. Wei *et al.*[16] used a method based on the lensing effect caused by refraction to obtain the wavelength of surface waves.

Space–time methods with "global imaging" and characterization of surface waves are not widely used. Zhang[17] used a refracted light beam to measure the surface gradient along a line. The surface gradient can then be integrated to obtain a surface topography. The issue of ambiguity in inverse mapping is avoided by using color coded light beams. Another approach based on comparing an image of a randomly generated pattern (for a disturbed interface) with a reference pattern (for an undisturbed fluid interface) is suggested by Moisy *et al.*[18] A DIC (digital image correlation) algorithm was used to extract the displacement field at every point in the image, quite similar to PIV (particle image velocimetry). Numerical integration of inverse gradient operator was performed to reconstruct the whole 2D surface topology. High curvature values cause the crossing of refracted rays from the pattern, and this cannot be handled by the DIC algorithms. This poses a limitation on the surface curvature the method can reconstruct. Liu *et al.*[19] used complex optical coherence tomography (OCT) to reconstruct the surface with a small field of view of 10×10 mm^2 and a penetration depth of 3.6 mm. Shao *et al.*[20] used a light intensity plot from reflected images to obtain a crude mapping of wave amplitude of the whole surface. Slavchov *et al.*[5] developed a refraction-based method to reconstruct the complete surface. This method requires a very regular plane surface wavefront and relies on prior knowledge of an analytical solution as a cost function for data fitting.

A new method is proposed in this work to reconstruct the surface of capillary waves along a representative selected straight line where a "laser sheet" hits the surface. The method was developed to be included easily in lab sessions of academic institutions and it is based on very limited and generic assumptions whose validity can be ensured during the experimental validation. This method can be classified as partially global (space–time) and is based on inverse ray-tracing of the refracted "laser sheet," which is refracted through the interface and projected down onto a screen. Mathematical formulations and solutions of forward and inverse problems in geometric optics are explained in depth in this paper.

II. METHODOLOGY

Refraction can be defined as the angular deviation of light rays when passing from one medium to another. The French mathematician Pierre de Fermat (1607–1665) put forth his famous principle based on "least time" to explain this phenomenon.

For a simpler case as shown in Fig. 2, Snell's law relates the angle of incidence and the angle of refraction as follows:

$$\frac{\sin(\Theta_i)}{\sin(\Theta_r)} = \frac{V_1}{V_2} = \mu_{1,2}. \tag{1}$$

Here, Θ_i is the angle of incidence, Θ_r is the angle of refraction, V_1 is the velocity of light in medium 1, V_2 is the velocity of light in medium 2, and $\mu_{1,2}$ is the refractive index for the pair of media 1–2.

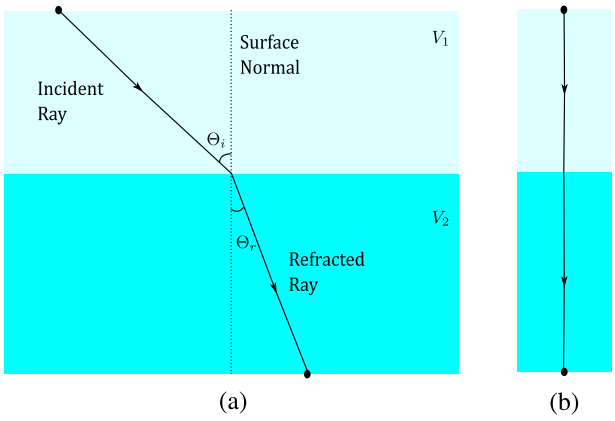

FIG. 2. Refraction of light in 2D. (a) Representation of Snell's law (front view). (b) Coplanarity of incident ray, refracted ray, and surface normal (side view).

A detailed description of Fig. 2 and derivation of Eq. (1) is found in Hecht.[21] The light rays move toward or away from the normal based on the refractive index of the media. If the surface is wavy, the surface normal and, hence, the direction of refracted rays also change over space and time. The angular deviation depends on several factors such as the refractive index of the material, the angle of incidence, and the direction of the surface normal. Where the ray may hit a bottom or a screen also depend on the fluid depth. This well-known phenomenon and simple observation can be used to exploit the interfacial wave. With sufficient and suitable distance from the surface to a projection screen, even tiny light ray deviations can be detected and measured. The surface disturbances caused by capillary surface waves can then be clearly monitored and measured. As a historical analog could be mentioned the first optical aided ("light ray and mirror") electric galvanometers.

A. Forward problem: Formulation

Consider the surface of a liquid filled cylindrical vessel. Capillary waves can then be generated by external mechanical excitation, e.g., a thin needle oscillating up and down. Placed at the geometric center of the vessel, a radial symmetric surface wave can be produced. The use of a "laser sheet" enables studying light refraction through the liquid interface. A "laser sheet" is produced by letting a laser beam be expanded sideways by passing through a cylindrical lens. This method is also used in particle image velocimetry (PIV) for the study of fluid flow velocity profiles. Now, a continuous laser line is pointing along the surface rather than just through a single hitting point. The laser sheet assembly can be moved and oriented in any direction. The light sheet undergoes refraction at two locations: at the air–liquid interface at the top and then again at the liquid–glass–air interface at the bottom. The modified laser sheet exiting the glass bottom is then projected onto a screen placed below the vessel. To simplify the mathematical analysis, the cylindrical vessel is assumed to be just a passive surface confining the fluid. Thus, the extra optical refraction caused by glass walls and bottom is neglected. However, for analysis and interpretation of real experiments, the glass bottom has to be included. The distance from the bottom of the vessel to the screen determines the optical spread of the laser sheet. A conceptual setup is shown in Fig. 3. The origin of the Cartesian coordinate frame is at point o, and vectors representing the location are shown with dots and vectors representing the direction are shown with arrows.

The generated capillary waves are not stationary; of course, they propagate radially out from the excitation center. In the radial symmetric case, the wave surface height z is a function of radial position (r) and time (t). In general, using the Cartesian coordinates x and y, the wave height z can be represented using a scalar function as follows:

$$z = z(x, y, t).$$

Here, z is the height of the capillary wave.

For purpose of analysis, consider waves "frozen" in time. This can be ensured experimentally by capturing the images at high speed and short shutter times. With this assumption, the "forward problem" of calculating a ray tracing from the light source to the screen has a unique solution for a given surface at a given time. The "frozen" surface can now be represented as

$$z = z(x, y).$$

The $z : \mathbb{R}^2 \to \mathbb{R}$ is converted into $f : \mathbb{R}^2 \to \mathbb{R}^3$ as follows:

$$\vec{f}(x, y) = \begin{bmatrix} x \\ y \\ z(x, y) \end{bmatrix}. \tag{2}$$

We represent the surface in such a way that it simplifies the calculation of the surface normal. The position of the laser source and inclination of the outgoing laser sheet is assumed to be known. For computational simplicity, the laser sheet is assumed parallel to the y axis. The "forward problem," i.e., the propagation of light from the source to the bottom and the screen is described as follows:

Known parameters:

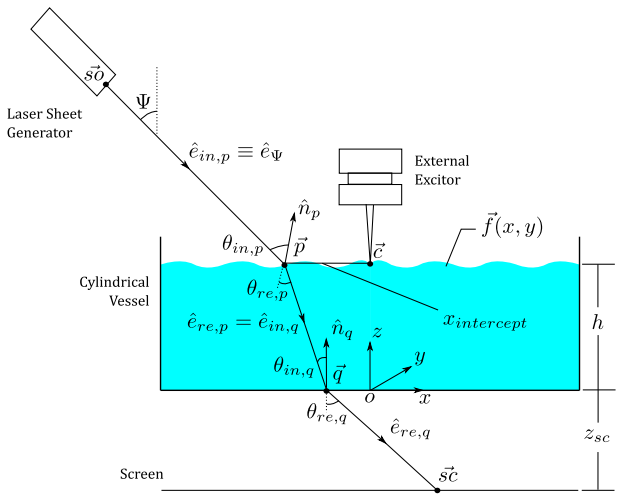

FIG. 3. Schematic illustration of the experimental setup for calculation of the forward problem.

- surface topography (assumed as a model surface) ($\vec{f}(x,y)$),
- laser location ($\vec{so} = [x_{so},\ y_{so},\ z_{so}]^T$),
- laser sheet inclination (Ψ),
- refractive index of the fluid ($\mu_{1,2}$),
- the undisturbed (no wave) height of the liquid (h), and
- distance between screen and bottom of the vessel (z_{sc}).

Unknown parameters:

- screen coordinates illuminated by the doubly refracted ray ($\vec{sc} = [x_{sc},\ y_{sc},\ z_{sc}]^T$).

Forward problems of this kind, as mentioned above, are famously known as ray-tracing in the geometric optics and computer graphics community.

B. Forward problem: Solution

The assumptions used for solving the forward problem are as follows:

1. The liquid is transparent and Newtonian.
2. The complete system is isothermal, thus the liquid has a constant refractive index.
3. Light rays travel in a straight line while traveling in the same medium.
4. A laser sheet is used as a light source.
5. Snell's law governs the refraction of rays at the interface.
6. Only light refraction is considered. We may neglect the effect of light reflection since the reflected rays from low amplitude waves will not propagate as secondary rays through the liquid. Thus, they will not hit the bottom screen.

This problem is solved numerically with a MATLAB script. The linear laser sheet is discretized as a dense set of individual rays in the y-direction. As the individual rays hit the surface, they are traced further through various media and interfaces until they reach the screen at the bottom.

To calculate the coordinates of the ray-liquid intersection point, an emitted ray is starting from the laser source ($\vec{so}$) in the given direction (Ψ). The ray then propagates along its directional unit vector ($\hat{e}_\Psi$). By definition,

$$\hat{e}_{in,p} \equiv \hat{e}_\Psi,$$

and, thus,

$$\vec{p} = (\vec{so} + \eta\ \hat{e}_{in,p}). \tag{3}$$

Here, η is the scale factor, i.e., the ray length from the source to the interface, and $\hat{e}_{in,p}$ is the unit vector in the direction of an incident ray.

The scale factor (η) shown in Fig. 4 corresponds to the intersection of a ray with the wave surface, which is obtained by solving,

$$\left((\vec{p} - \vec{f}(x,y)) \cdot \hat{e}_z\right) = 0. \tag{4}$$

Here, $\vec{p}$ is the intersection point of an incident ray with the wave surface and $\hat{e}_z$ is the unit vector in the z-direction (pointing upward).

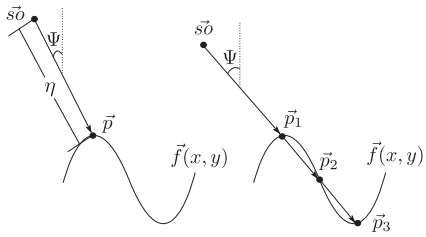

FIG. 4. Valid solutions of surface intersection point ($\vec{p}$) based on wave curvature, inclination of laser source (Ψ), and initial guess values for solving Eq. (4).

In principle and mathematically, several ray lengths (η) are possible and "valid" in case of large angle of incidence, or at high wave curvature. This would be due to multiple intersections as shown in Fig. 4. However, in real physics, only the "first hit," i.e., the shortest ray length, is of importance. To avoid ambiguity, the initial guess value for the solver is chosen judiciously.

The surface normal vector at the intersection point is evaluated using the following equation:

$$\begin{aligned} \vec{n}_p &= \left(\frac{\partial \vec{f}}{\partial x}\right)\Big|_{\vec{p}} \times \left(\frac{\partial \vec{f}}{\partial y}\right)\Big|_{\vec{p}}, \\ \vec{n}_p &= -\left(\frac{\partial z}{\partial x}\right)\hat{i} - \left(\frac{\partial z}{\partial y}\right)\hat{j} + \hat{k}, \end{aligned} \tag{5}$$

and then normalized as

$$\hat{n}_p = \frac{\vec{n}_p}{|\vec{n}_p|}. \tag{6}$$

Here, $\vec{n}_p$ is the surface normal evaluated at the intersection point ($\vec{p}$); $\hat{n}_p$ is the unit vector corresponding to $\vec{n}_p$; $\hat{i}, \hat{j}$, and $\hat{k}$ are the unit vectors along x, y, and z axes, respectively.

Afterward, the angle of incidence is calculated followed by the angle of refraction using Snell's law as follows:

$$\theta_{in,p} = \arccos(\hat{n_p} \cdot (-\hat{e}_{in,p})), \tag{7}$$

$$\theta_{re,p} = \arcsin\left(\frac{\sin(\theta_{in,p})}{\mu_{1,2}}\right). \tag{8}$$

Here, $\theta_{in,p}$ is the angle of incidence at point of intersection ($\vec{p}$) and $\theta_{re,p}$ is the angle of refraction at point of intersection ($\vec{p}$).

As shown in Fig. 3, the unit incident vector ($\hat{e}_{in,p}$) points downward. Thus, a flipped vector ($-\hat{e}_{in,p}$) is used in Eq. (7) to obtain the desired angle ($\theta_{in,p}$) value with respect the to the direction of surface normal ($\hat{n}_p$). Note that the laser sheet inclination angle (Ψ) is fixed but the angles are calculated in Eqs. (7) and (8) change depending on the curvature at the point of intersection ($\vec{p}$). By referring to Fig. 2, the direction of the refracted ray is calculated by using the coplanarity of the incident ray, surface normal, and the refracted ray,

$$\hat{e}_{re,p} = \alpha_1 \hat{e}_{in,p} + \beta_1 \hat{n}_p. \tag{9}$$

Here, $\hat{e}_{re,p}$ is the unit vector in the direction of the refracted ray corresponding to incident ray unit vector $\hat{e}_{in,p}$ at the point of intersection $(\vec{p})$,

$$\begin{aligned} \hat{e}_{in,p} \cdot \hat{e}_{re,p} &= \cos(\theta_{in,p} - \theta_{re,p}), \\ \hat{e}_{in,p} \cdot (\alpha_1 \hat{e}_{in,p} + \beta_1 \hat{n}_p) &= \cos(\theta_{in,p} - \theta_{re,p}), \\ \alpha_1 + \beta_1 \cos(\pi - \theta_{in,p}) &= \cos(\theta_{in,p} - \theta_{re,p}). \end{aligned} \tag{10}$$

$$\begin{aligned} \hat{e}_{re,p} \cdot \hat{n}_p &= \cos(\pi - \theta_{re,p}), \\ (\alpha_1 \hat{e}_{in,p} + \beta_1 \hat{n}_p) \cdot \hat{n}_p &= \cos(\pi - \theta_{re,p}), \\ \alpha_1 \cos(\pi - \theta_{in,p}) + \beta_1 &= -\cos\theta_{re,p}. \end{aligned} \tag{11}$$

A unit vector in the direction of the refracted ray is used here as an extra constraint to obtain unique values of $[\alpha_1,\ \beta_1]^T$. After putting Eqs. (10) and (11) in a matrix form, we get

$$\begin{bmatrix} \alpha_1 \\ \beta_1 \end{bmatrix} = \begin{bmatrix} 1 & -\cos(\theta_{in,p}) \\ -\cos(\theta_{in,p}) & 1 \end{bmatrix}^{-1} \begin{bmatrix} \cos(\theta_{in,p} - \theta_{re,p}) \\ -\cos(\theta_{re,p}) \end{bmatrix}. \tag{12}$$

Equation (12) will not yield a unique solution in the case where

$$\theta_{in,p} = \theta_{re,p} = 0.$$

This issue has to be included in the MATLAB script. The refracted ray is then traced inside the fluid until it hits the bottom of the vessel. A similar procedure is repeated at the fluid–air interface to obtain the intersection point $(\vec{q})$, the angle of incidence $(\theta_{in,q})$, the angle of refraction $(\theta_{re,q})$, and finally the direction of refracted ray $(\hat{e}_{re,q})$. Bottom being a flat surface,

$$\hat{n}_q = \hat{e}_z.$$

Here, $\hat{n}_q$ is the unit surface normal evaluated at the point of intersection of an incident ray with the vessel bottom.

Subsequently, the refracted ray is traced until it hits the screen $(\vec{sc})$. Ray-tracing simulations for typical wave surface topographies are presented in Sec. III.

C. Inverse problem: Formulation

Solving the forward problem is important in several ways. First, it provides insight into the mathematical operations involved and clarifies the known and unknown parameters for the inverse problem. We then also obtain data for various input parameter combinations, which can be compared with the solution of the inverse problem (referred to as the true wave shape in Sec. III). Generally, inverse problems are investigated in two steps:

- existence of a unique solution and
- method of finding that unique solution.

Finding and reconstructing the wave surface topography requires knowledge of coordinates of surface point (x- and y-coordinates, i.e., two unknowns) and also associated surface normal (three unknowns). The number of unknowns in defining surface points can be reduced by one by assuming that the x-coordinate $(x_{intercept})$ of the intersection point of rays and surface is known. As assumed previously, the use of a laser sheet as a light source parallel to the y axis reduces this coordinate to just one number. Since this parameter can be easily measured and controlled, this simplification is compatible with experimental aspects. Similarly, the number of unknowns in defining a surface normal can be further reduced by one by assuming a unit length. Finally we have,

- total unknown parameters: 3 (wave surface y-coordinate, i.e., one unknown, surface normal direction angles, i.e., two unknowns),
- total known parameters: 2 (screen x- and y-coordinates),

$$(unknown\ parameters) > (known\ parameters). \tag{13}$$

Thus, it can be deduced from Eq. (13) that there exist multiple valid solutions. To define a well-posed problem and obtain a unique solution from the set of all valid solutions, the axisymmetric nature of the wave surface is used as a constraint.

In Fig. 5, surface normals can be seen tilting toward/away from the radius vector (vector pointing from the point of excitation, the center, toward the point of intersection on the wave surface). Mathematically, this means that the surface normals at all points lie in the plane spanned by the corresponding radius vector and the unit vector in the z-direction (coplanarity) as explained in Fig. 7. This fact will be used as a constraint to find the best fit surface normal from a set of possible solutions.

The schematic experimental setup for the inverse problem is almost identical to Fig. 3. The point contact between the probe and the fluid surface shown in the schematic setup ensures the axisymmetric nature of the wave surface topography. This is also possible to replicate in experiments, thus making it a valid assumption.

Known parameters:

- screen coordinates illuminated by the doubly-refracted ray $(\vec{sc} = [x_{sc},\ y_{sc},\ z_{sc}]^T)$,
- laser location $(\vec{so} = [x_{so},\ y_{so},\ z_{so}]^T)$
  or
  laser sheet inclination (Ψ),
- height of fluid in quiescent state (h),

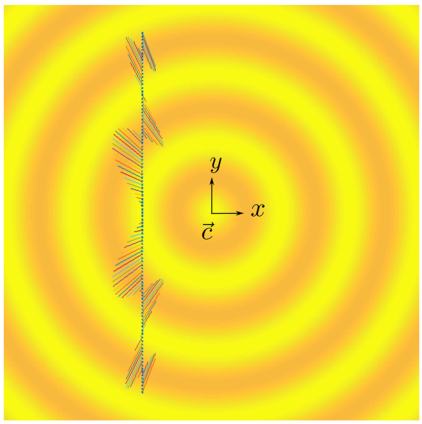

FIG. 5. Surface normals for axisymmetric waves tilt toward or away from the exciter center (top view projection).

- coordinates of point of excitation ($\vec{c} = [0,\ 0,\ h]^T$),
- distance between the center and the illuminated line on wave surface topography along x axis ($x_{intercept}$),
- refractive index of the Newtonian fluid ($\mu_{1,2}$), and
- distance between the plane of the screen and the bottom of the vessel (z_{sc}).

Unknown parameters:

- wave surface topography cross-section ($z(x_{intercept}, y)$).

Interestingly, the knowledge of either the laser location ($\vec{so}$) or the laser inclination (Ψ) is required for solving the inverse problem. The reason for this is explained after Eq. (18). We choose the latter as this makes the placement of the laser source easier and more flexible in an experimental setup.

D. Inverse problem: Solution

In addition to assumptions used in the solution of the forward problem, the following assumptions are used while solving the inverse problem:

1. Wave surface topography is axisymmetric.
2. Laser sheet hits the wave surface parallel to y axis and x-coordinate of the location where rays that hit the wave surface ($x_{intercept}$) have one value.
3. The origin of the Cartesian coordinate frame is at point o in Fig. 3.

For the inverse problem, a ray is imagined to travel from a point on the screen toward the laser source as shown in Fig. 6. This changes the perceived directions of incident and refracted rays accordingly. Initially, the wave surface is approximated as flat. Thus, the deviation

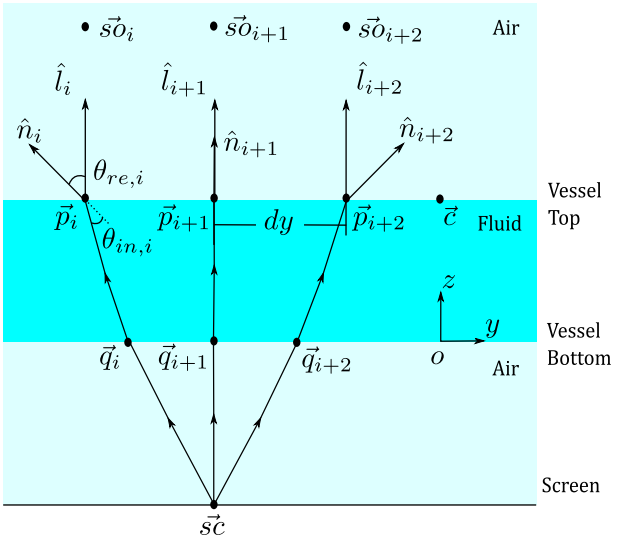

FIG. 6. 2D schematic of inverse problem solution. Point $\vec{c}$ is the excitation center. The reconstruction is, as here for a start, assuming a flat surface. However, the reconstructed surface normals are found to be inclined, so these are used for constructing the whole wavy surface by integration. See the text for more explanation.

in the ray path can be assumed to be caused solely by the changing the direction of surface normals. This problem is also solved numerically with a MATLAB script. The laser sheet line segment impinging on the flat fluid surface is discretized, and this results in nodes ($\vec{p}_i$) along the y-direction (Figs. 3 and 5). The discretized element size (dy) must be chosen accordingly considering the trade-off between accuracy and computation time. The choice of element size is observed to have a significant effect on the computation time (Sec. III D). The whole inverse problem then reduces to finding the unique direction of the unit surface normal at a given discretized node for which a ray starting at a given point on screen ends up following a path toward the source of the laser sheet after the two interface refractions. As explained in Sec. II C, several valid solutions to this problem are possible, depending on the laser sheet inclination and the wave steepness. This means that for each point on screen ($\vec{sc}$), a valid direction of unit surface normal ($\hat{n}_i$) is obtained corresponding to each discretized node ($\vec{p}_i$) on the fluid surface. From all identified solutions, the unique solution is chosen by applying the constraint of axisymmetry. After this, the cross-section of the wave surface is reconstructed.

Note that the inverse modeling starts with the assumption of an initial flat fluid surface in Fig. 6. Consider coordinates of a point on screen ($\vec{sc} = [x_{sc},\ y_{sc},\ z_{sc}]^T$) and ith discretized node on the assumed flat surface ($\vec{p}_i = [x_{intercept},\ y_i,\ h]^T$). It can be clearly seen in Fig. 6 that the point of intersection of a ray (travelling "backward" toward $\vec{p}_i$ from $\vec{sc}$) with bottom of vessel ($\vec{q}_i = [x_q,\ y_q,\ 0]^T$) is calculated using Fermat's principle of least time mentioned in Sec. II. The total time taken by a ray to travel from $\vec{sc}$ to $\vec{p}_i$ is given by

$$\tau = \frac{|(\vec{q}_i - \vec{sc})|}{V_1} + \frac{|(\vec{p}_i - \vec{q}_i)|}{V_2}. \tag{14}$$

Here, τ is the total time taken by a ray to travel from $\vec{sc}$ to $\vec{p}_i$, V_1 is the velocity of light in air (constant), and V_2 is the velocity of light in fluid (constant).

After substituting Eq. (1) in the above equation and rearranging, we get

$$\tau V_2 = \frac{|(\vec{q}_i - \vec{sc})|}{\mu_{1,2}} + |(\vec{p}_i - \vec{q}_i)|. \tag{15}$$

Since the z-coordinate of $\vec{q}_i$ is known, minimum travel time is ensured by solving for the remaining two unknowns i.e., x- and y-coordinates (x_q and y_q) as follows:

$$\arg\min_{\vec{q}_i} \left(\frac{|(\vec{q}_i - \vec{sc})|}{\mu_{1,2}} + |(\vec{p}_i - \vec{q}_i)| \right). \tag{16}$$

Here, $\vec{q}_i$ is the intersection of the ray with vessel bottom.

Now, the surface normal ($\hat{n}_i$) at $\vec{p}_i$ is calculated so that the ray coming from the screen ($\vec{sc}$) follows the path toward the source of the laser sheet ($\vec{so}_i$). Consider a dummy vector ($\vec{l}_i$) representing the refracted ray (travelling from $\vec{p}_i$ toward $\vec{so}_i$) that points in the same direction. Since the rays from the laser source travel parallel to the x-axis, $\vec{l}_i$ is defined as

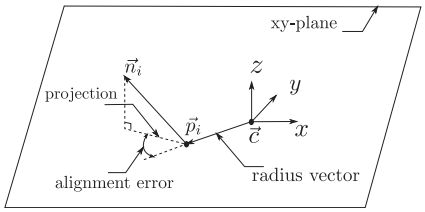

FIG. 7. Finding the best fit surface normal corresponding to a given point on the interface using the coplanarity constraint.

$$\vec{l}_i = \sigma \begin{bmatrix} -\sin(\Psi) \\ 0 \\ \cos(\Psi) \end{bmatrix}. \tag{17}$$

Here, σ is the scalar factor (=1 for simplicity).

If the position of the laser source is known, then the same vector is represented as

$$\vec{l}_i = \vec{so}_i - \vec{p}_i. \tag{18}$$

It can be verified that Eqs. (17) and (18) are just scaled versions of each other and, thus, are equivalent. Since $\vec{l}_i$ is a proxy for the refracted ray pointing toward the laser source, there is no need to know the location of the laser source ($\vec{so}$) for further analysis.

Using the coplanarity mentioned in Fig. 2, the surface normal ($\hat{n}_i$) lies in the span of incident ray and (dummy) refracted ray,

$$\hat{n}_i = \alpha_2(\widehat{\vec{q}_i - \vec{p}_i}) + \beta_2(\widehat{\vec{l}_i - \vec{p}_i}).$$

Here, $\hat{n}_i$ is the surface normal corresponding to $\vec{p}_i$.

Surface normal that satisfies Snell's law is obtained by solving for α_2 and β_2 as follows:

$$\theta_{in,i} = \arccos -\hat{n}_i \cdot (\widehat{\vec{q}_i - \vec{p}_i}), \tag{19}$$

$$\theta_{re,i} = \arccos(\hat{n}_i \cdot \hat{l}_i), \tag{20}$$

$$\underset{\alpha_2,\ \beta_2}{\arg\min}\ |\mu_{1,2}\ \sin\theta_{in,i} - \sin\theta_{re,i}|. \tag{21}$$

The flipped vector ($-\hat{n}_i$) is used in Eq. (19) to obtain the desired angle ($\theta_{in,i}$) value with respect the to the direction of the surface normal. Since all scalar multiples of $\hat{n}_i$ are a valid solution, the unit surface normal is used in Eqs. (19) and (20), which ensures unique values of α_2 and β_2.

A ray of light starting from a point on the screen ($\vec{sc}$) and passing through points $\vec{q}_i$ and $\vec{p}_i$ will follow a path toward the corresponding laser source location ($\vec{so}_i$) only for a unique surface normal direction ($\hat{n}_i$) as calculated in Eq. (21). We obtain these valid unit surface normals for all points on the surface of wave ($\vec{p}_i$) corresponding to the single point on the screen ($\vec{sc}$). Out of these, the desired points ($\vec{p}_i$ and $\vec{q}_i$) and associated surface normal ($\hat{n}_i$) is chosen by invoking the axisymmetric assumption about the nature of the waves. The coplanarity of the unit surface normal, radius vector, and the unit vector in the z-direction (located at the center) is used as a filter (Fig. 5). For a valid solution, the vector of the projection of $\hat{n}_i$ on the xy plane must be collinear with the corresponding radius vector ($\vec{p}_i - \vec{c}$) (Fig. 7). The following shows one of the ways to quantify the error in the alignment:

$$\underset{\vec{p}_i,\ \hat{n}_i}{\arg\min}\ |((\widehat{\vec{p}_i - \vec{c}}) \times \hat{e}_z) \cdot \hat{n}_i|. \tag{22}$$

Here, $\vec{c}$ is the vector for the coordinates of center, i.e., point of excitation.

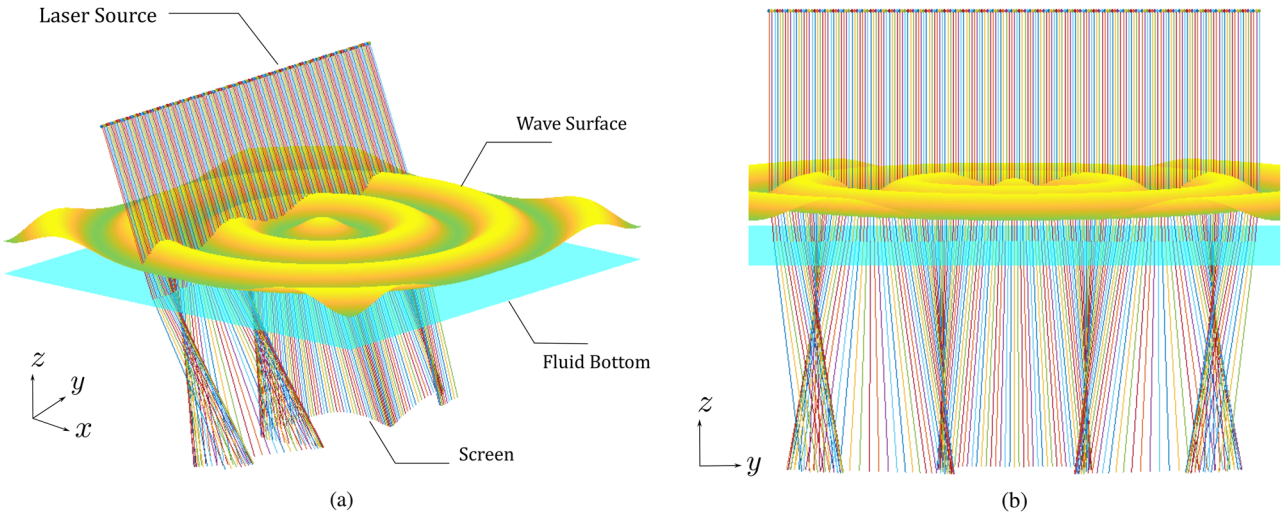

FIG. 8. Numerical simulation of the forward problem of undamped surface wave (the wave amplitude here and in later plots is exaggerated for better visualization). (a) Oblique front view. (b) Front view toward the laser sheet.

TABLE I. List of parameters with base values.

Parameter	Value	Unit
Ψ	0	deg
λ	5	mm
a	0.5	mm
$x_{intercept}$	−0.5	mm
dy	0.25	mm
k	0	⋯
h	5	mm
$\mu_{1,2}$	1.33	⋯
z_{sc}	150	mm

Thus, based on the coplanarity requirement, Eq. (22) is used to find the best fit. This algorithm is repeated for all subsequent points on the screen to reconstruct the corresponding points on the surface and associated surface normals. Now, the resulting surface normals suggest a non-flat surface that contradicts previous approximation as expected.

As suggested, the output of Eq. (22) is unit surface normals, whereas surface normals are required for the reconstruction of the surface [Eqs. (23)–(25)]. It can be easily observed in Eq. (5) that the length of the surface normals can be recovered by taking a reciprocal of the $\hat{k}$ coefficient of the unit surface normal as follows:

$$|\vec{n}_i| = \frac{1}{(\hat{n}_i \cdot \hat{e}_z)}. \tag{23}$$

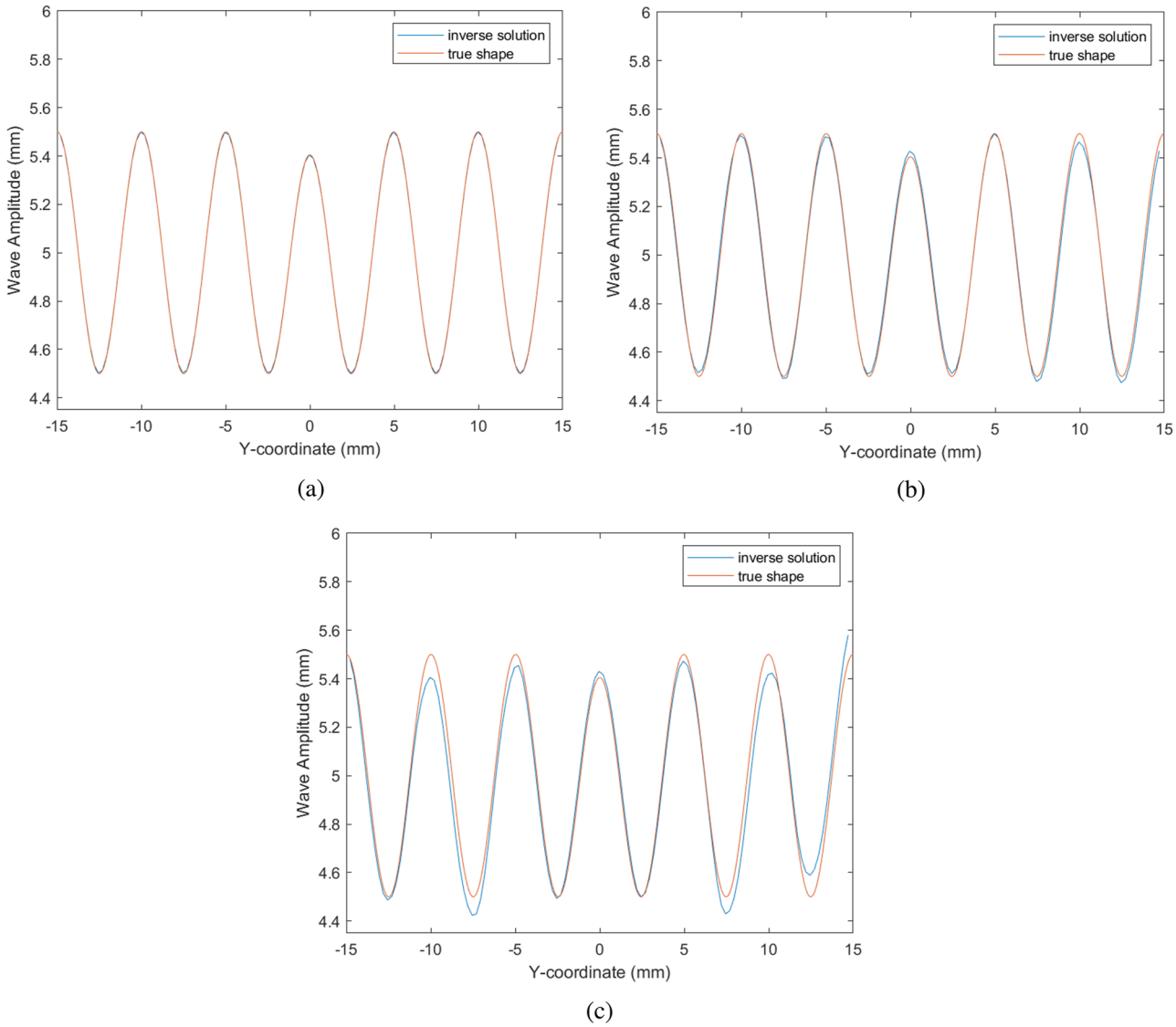

FIG. 9. Effect of Ψ on the reconstructed cross-section of wave topography. (a) $\Psi = 0°$. (b) $\Psi = 10°$. (c) $\Psi = 20°$.

This length value is then used to scale the unit surface normals, which yields the actual surface normal values. The surface gradient in the y-direction is obtained by taking the $\hat{j}$ coefficient of Eq. (5). Thus, we get the actual gradient in the y-direction as follows:

$$\frac{\partial z}{\partial y} = -(\hat{n}_i \ |\vec{n}_i|) \cdot \hat{e}_y. \tag{24}$$

Here, $\hat{e}_y$ is the unit vector in the y-direction.

To recreate the cross-section of this non-flat surface topography, numerical integration (Simpson's 1/3rd method) and cubic interpolation (for intermediate values) are carried out in the y-direction as follows:

$$z(x = x_{intercept}, y) = \int_{y=y1}^{y=y2} \frac{\partial z}{\partial y}\, dy. \tag{25}$$

Here, y_1, y_2 are the y-axis limits of the illuminated line segment on the wave surface and dy is the distance between successive discretized nodes in the y axis.

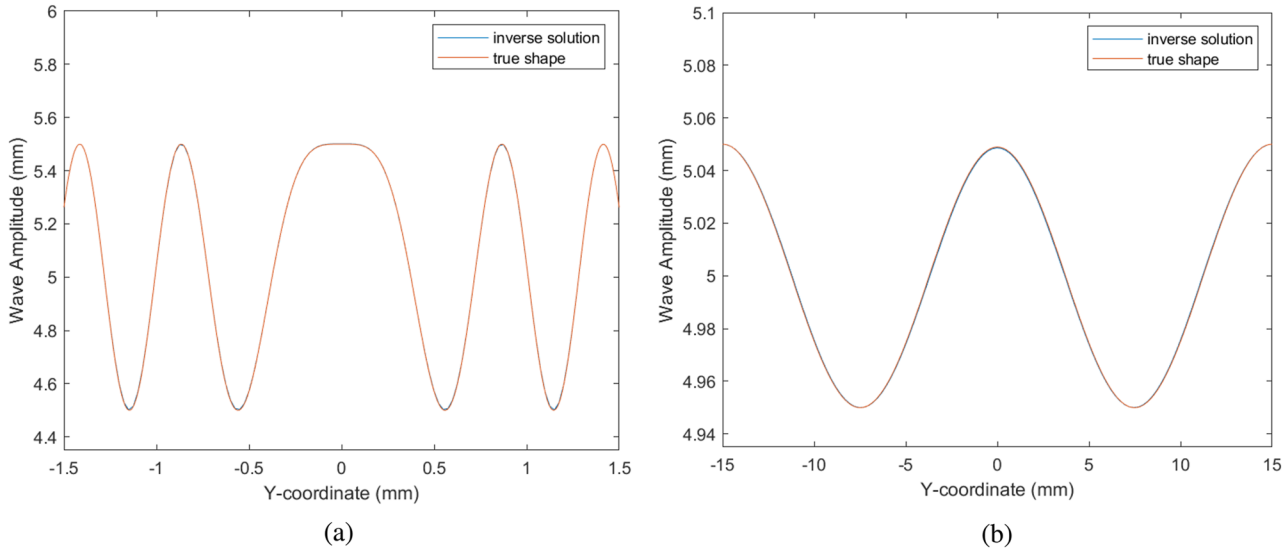

FIG. 10. Effect of wave parameters of undamped wave on the reconstructed cross-section of wave topography. (a) $\lambda = 0.5$ mm, $a = 0.5$ mm, $dy = 0.025$ mm, $k = 0$. (b) $\lambda = 15$ mm, $a = 0.05$ mm, $dy = 0.25$ mm, $k = 0$.

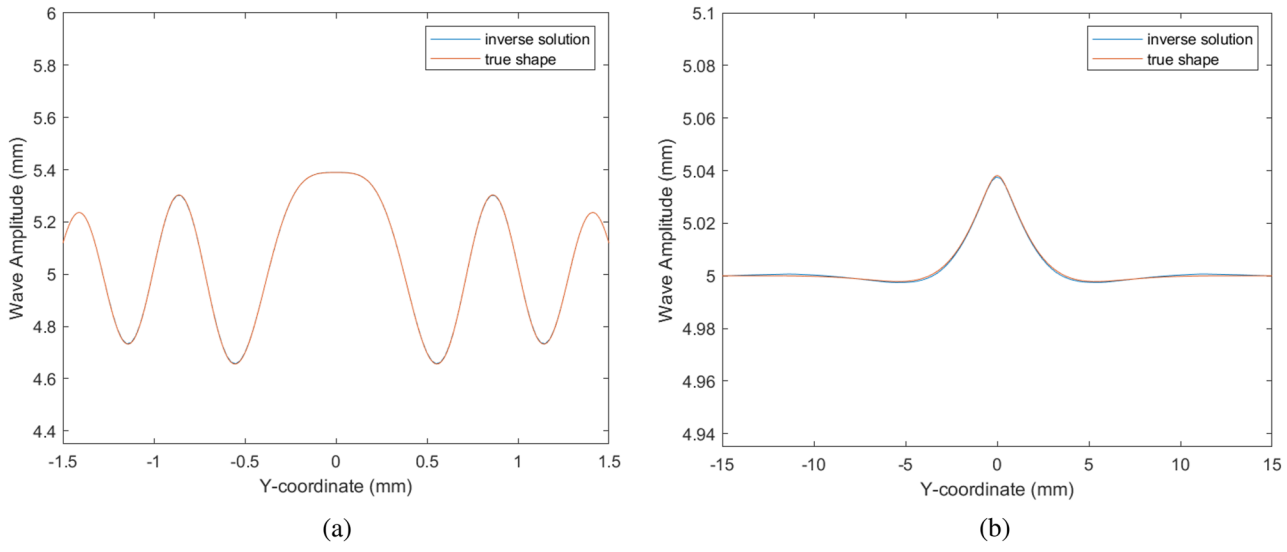

FIG. 11. Effect of wave parameters of damped wave on the reconstructed cross-section of wave topography. (a) $\lambda = 0.5$ mm, $a = 0.5$ mm, $dy = 0.025$ mm, $k = -0.5$. (b) $\lambda = 15$ mm, $a = 0.05$ mm, $dy = 0.25$ mm, $k = -0.5$.

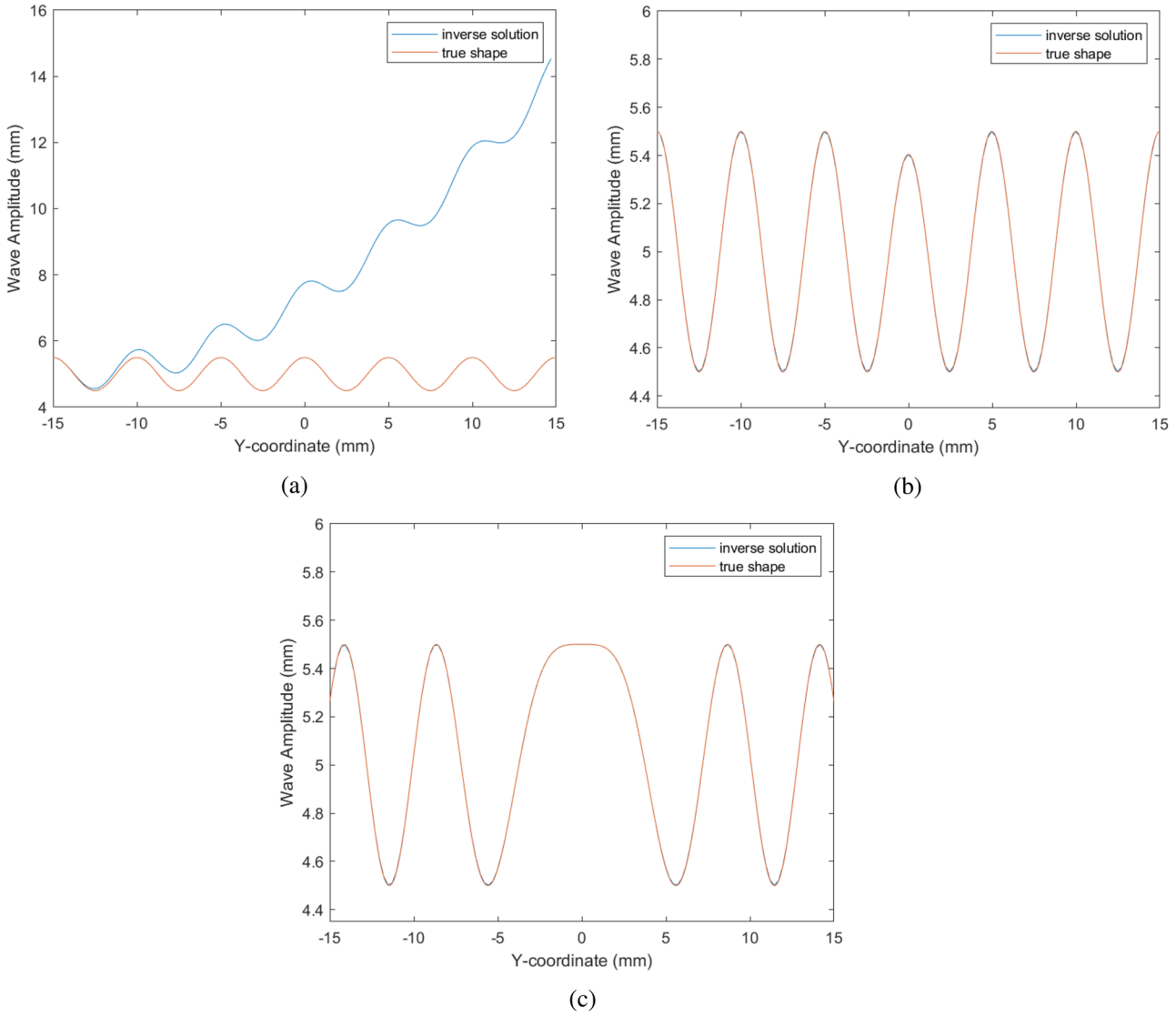

FIG. 12. Effect of $x_{intercept}$ on the reconstructed cross-section of wave topography. (a) $x_{intercept} = 0$ mm. (b) $x_{intercept} = -0.5$ mm. (c) $x_{intercept} = -5$ mm.

This is the numerical integration of an inverse gradient operator along only one direction (y-axis). Even though running the algorithm for a sequence of points on the screen yields corresponding points on the surface of the fluid, they are not necessarily sequential. Hence, sorting of data according to the y-coordinate is mandatory because sequential information about the surface normals is required for the numerical integration. The resulting surface topography will be shifted in the z-direction due to lack of initial condition (constant of integration). Although these data are sufficient for the purpose of our studies, the initial condition might be obtained by integrating the wave surface topography to match the initial volume of the vessel. For simplicity of comparison, the initial value from the solution of the forward problem is used in Sec. III.

The complete reconstruction of the wave surface height profile is carried out by measuring the distance (radius) of point $\vec{p}_i$ from the center of the waves ($\vec{c}$) and then assigning the corresponding z value to all points lying on the same radius, creating an axisymmetric wave surface.

III. RESULTS AND DISCUSSION

The methods for solving the forward and inverse problems are validated using numerical simulations. Even though the forward problem is not the focus of this paper, the results of the simulation for two different waveforms (damped and undamped) are presented

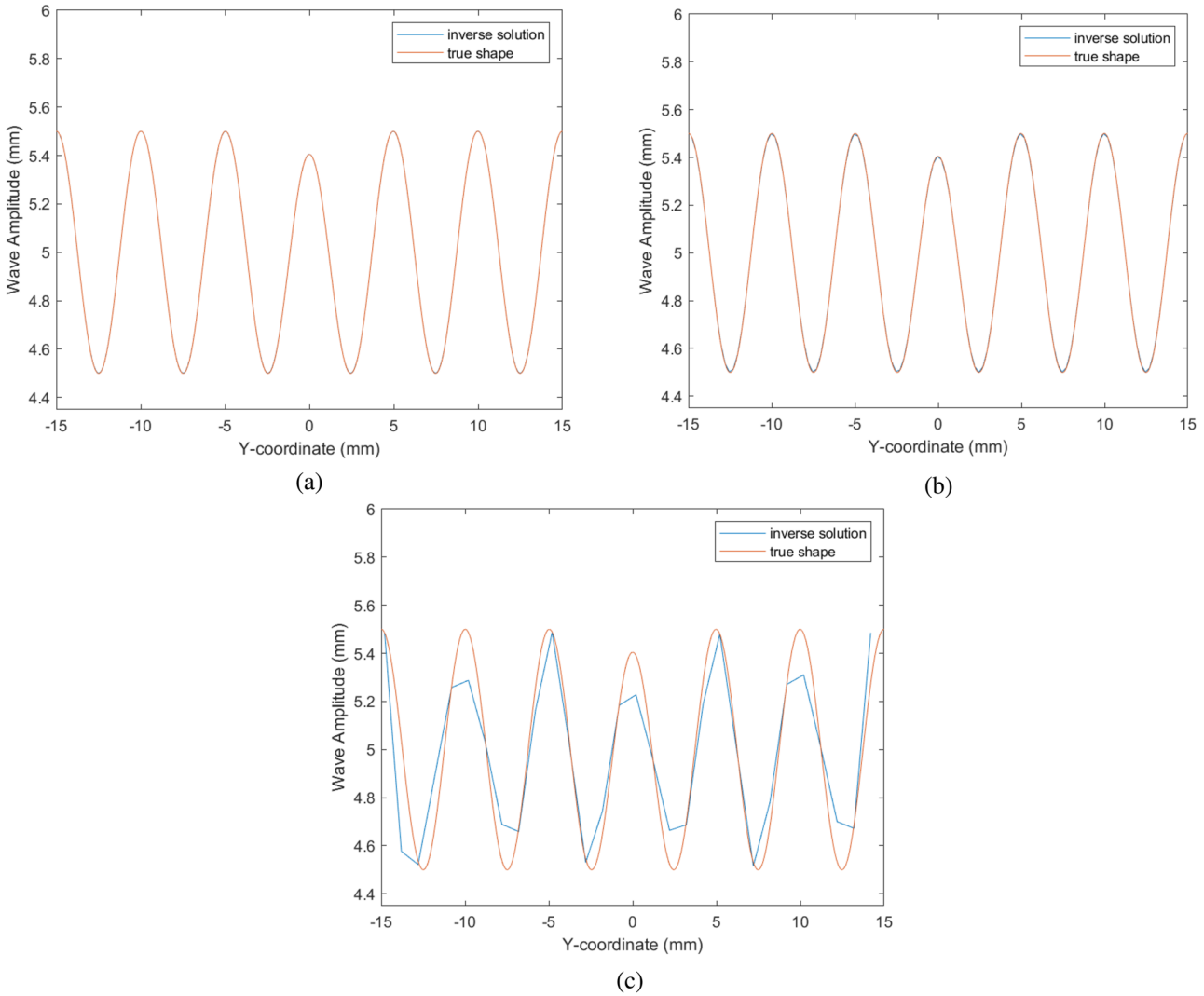

FIG. 13. Effect of *dy* on the reconstructed cross-section of wave topography. (a) $dy = 0.1$ mm. (b) $dy = 0.25$ mm. (c) $dy = 1.0$ mm.

below. Since the amplitude of capillary waves in real situations falls off with increasing radius, one example each of a wave with damped and undamped wave surface is considered. The lensing effect due to the surface curvature is observed in Fig. 8.

TABLE II. Error values for the reconstructed cross-section of wave topography with different values of Ψ.

	Error	
Ψ (Deg)	Average (%)	Maximum (%)
0	0.07	0.22
10	3.68	10.93
20	9.22	23.48

Various parameters that might affect the error values in the reconstruction of the cross-section of capillary wave surface topography in the inverse problem solution are mentioned in Table I. The wave topography considered for this analysis is

$$z(x,y) = h + a\ \cos\left(\frac{2\pi r}{\lambda}\right)e^{kr}. \tag{26}$$

Here, h is the fluid depth, a is the amplitude of the surface wave, $r = \sqrt{x^2 + y^2}$, λ is the wavelength of the surface wave, and k is the attenuation constant $(k \leq 0)$.

The base values of parameters for the simulation are shown in Table I. To gauge the effect of each parameter at a time, others are kept at base value during the analysis (except for the case of the effect of wave parameters). These effects of varying one parameter at a time

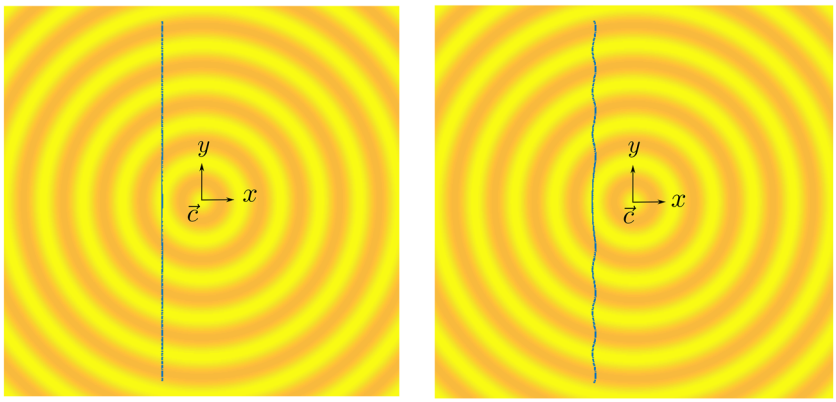

(a) (b)

FIG. 14. Coordinates of the intersection of laser sheet with the wave surface for different inclination angles (Ψ). (a) Ψ = 0°. (b) Ψ = 20°.

are analyzed in the following sections. The reference analytical surface obtained from Eq. (26) is referred to as "true shape" in Figs. 9–12 and 13.

A. Effect of laser sheet inclination (Ψ)

It is clear from Table II and Fig. 9 that the inversion reconstruction error increases with increasing laser sheet inclination Ψ . The reason for this is that, at a higher inclination angle, even neighboring laser sheet rays do not necessarily hit the wave surface at the same x-coordinate value due to the curvature of the surface (Fig. 14). This causes a deviation from the assumption made for solving the inverse problem, i.e., that all the laser sheet rays hit the surface at a single x-coordinate ($x_{intercept}$) (Sec. II D). The errors induced by these effects are referred to as "error values."

B. Effect of wave parameters

The amplitude of surface capillary waves drops with increasing distance (Fig. 3) from the excitation center. There are two reasons for that: (1) specific energy loss by energy spread over a longer wavefront circumference and (2) viscous damping. Thus, it is required to verify the proposed method for both high and low values of the curvature (a/λ), and for both damped and undamped waves [Eq. (26)]. The results shown in Table III, Figs. 10 and 11 confirm that the proposed method works for all axisymmetric surfaces, damped and undamped.

Different values of dy are used to resolve the simulated wave of λ = 0.5 mm and a = 0.5 mm. It is clear from Table III that the proposed method works quite well for waves with a wide range of λ/a ratios (1–300).

C. Effect of $x_{intercept}$

$x_{intercept}$ is the distance along the x-axis between the point of excitation and the illuminated line where the laser sheet hits the wave surface (Fig. 3). In view of symmetry, only $x_{intercept}$ values on one side of the point of excitation are considered.

There is a substantial difference in the error values in cases of $x_{intercept}$ = 0 mm and $x_{intercept}$ = −0.5 mm as seen in Fig. 12 and Table IV. For $x_{intercept}$ = 0 mm and Ψ = 0°, all the surface normals (even though pointing in different directions) lie in the same plane. This results in the "amplification" (as mentioned in Sec. II A) in that same plane (Fig. 15). This causes an overlap of rays, which results in the loss of unique solution for the inverse problem. This behavior is caused by all surface normals lying on the same plane and is not expected for other values of Ψ. It can be seen in Fig. 16 that $x_{intercept}$ values close to 0 mm capture the amplitude data of larger surface areas. Thus, optimally, $x_{intercept}$ should be positioned close to the wave exciter.

The reason for this choice is to capture a maximum amount of wavefronts in order to reduce the reconstruction error. This is particularly important since the amplitude attenuates quite rapidly in actual fluids (Fig. 11).

TABLE III. Error values for the reconstructed cross-section of wave topography with different values of wave parameters.

			Error	
Wave type	λ (mm)	a (mm)	Average ($\times 10^{-2}$%)	Maximum ($\times 10^{-2}$%)
Undamped (k = 0)	0.5	0.5	10.85	21.17
Undamped (k = 0)	15	0.05	0.71	1.33
Damped (k = −0.5)	0.5	0.5	4.28	10.73
Damped (k = −0.5)	15	0.05	1.71	42.17

TABLE IV. Error values for the reconstructed cross section of wave topography with different values of $x_{intercept}$.

	Error	
$x_{intercept}$ (mm)	Average (%)	Maximum (%)
0.0	323.75	563.26
−0.5	0.07	0.22
−5.0	0.05	0.37

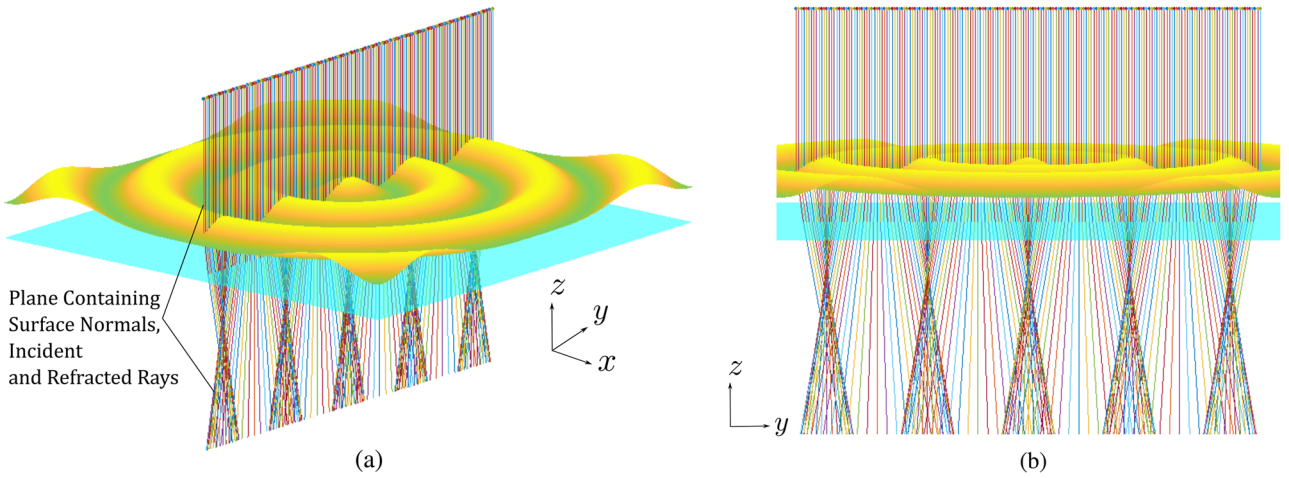

FIG. 15. Numerical simulation of the forward problem for $x_{intercept} = 0$ mm, i.e., crossing the exciter center, and $\Psi = 0°$, i.e., vertical laser sheet. (a) Oblique front view. (b) Front view toward the laser sheet.

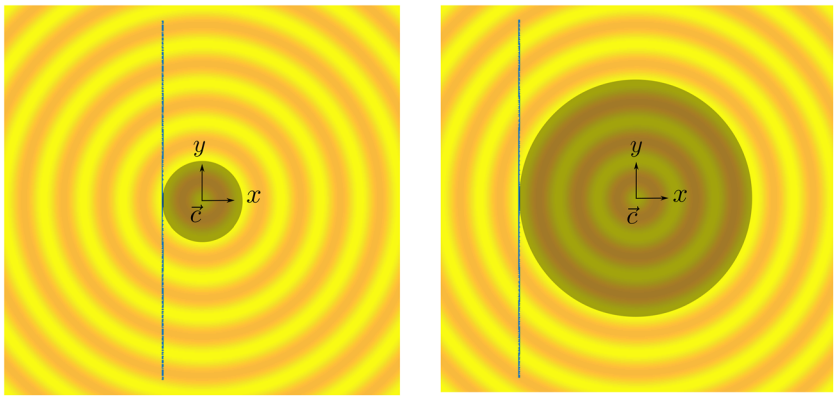

FIG. 16. The position of $x_{intercept}$ determines which wavefronts can be reconstructed: While still inside the darkened circle, wavefronts do not cross the laser sheet. Thus, they will not be projected onto the bottom screen until they move further out to cross the laser line. (a) $x_{intercept} = -5$ mm. (b) $x_{intercept} = -15$ mm.

D. Effect of size of discretized element (*dy*)

Sensitivity studies of the results with respect to domain discretization are essential in numerical simulations. Frequently, we see a trade-off between computation time and error values (Table V). The errors reduce quite drastically from $dy = 1.0$ mm to $dy = 0.25$ mm with a significant increase in the computation time. On the contrary, we see no significant improvement in the error values from $dy = 0.25$ mm to $dy = 0.1$ mm, while also introducing a substantial jump in computation time.

Even for coarse discretization, the inverse solution matches quite well with the ground truth in the middle part (Fig. 13). The error seems to be concentrated near peaks and valleys of the wave where the curvature value is high.

TABLE V. Error values for the reconstructed cross section of wave topography with different values of *dy*.

		Error	
dy (mm)	Computation time (s)	Average (%)	Maximum (%)
0.1	466	0.06	0.12
0.25	89	0.07	0.22
1.0	5	16.17	92.10

E. Effect of other variables

Other variables include the height of fluid (h), the distance of screen from the bottom (z_{sc}), and the refractive index $(\mu_{1,2})$. These variables are dictated by experimental feasibility and their role is limited to causing the "amplification" of the surface disturbances (Fig. 8). Moreover, they have no significant impact on the error values. These parameters are more important experimentally where the effective resolution of the points on the screen is critical.

IV. CONCLUSION

The capillary waves are characterized by very small values of amplitude, which makes it difficult to measure using intrusive meth-

ods. A non-intrusive method based on geometric optics is proposed to reconstruct the wave surface with very high accuracy. In this method, a laser sheet illuminates a wave surface and refracts by a varying degree based on the direction of the local surface normal (curvature). The forward problem is defined and solved to trace the rays of light following Snell's law. The data of refracted laser sheet are then used as an input to the inverse problem to obtain correct surface normals. This method exploits the axisymmetric nature of the wave surface to filter out the best fit surface normal from the available solutions for a given point on the interface to reconstruct the cross-section of the wave surface. Both forward and inverse problems are defined with reasonable assumptions, and solved numerically to obtain an excellent agreement in reference analytical (true shape) and reconstructed wave surfaces. This method can work with swapped positions of laser source and screen, and prove to be useful in studying axisymmetric surfaces in general.

Equations and assumptions used in the solution method are clearly explained. A parametric study is performed to understand the effects of various parameters on the error values in the reconstruction. Laser sheet inclination (Ψ) and the distance between the center and the illuminated line on wave surface topography along the x-axis ($x_{intercept}$) have a larger impact on the final result. $\Psi = 0°$ and $x_{intercept} \rightarrow 0$ mm are found to be the optimum values. The grid sensitivity study yields the usual trade-off between computation time and error values. Since the errors for coarse discretization are concentrated at the peaks and valleys of the wave surface cross-section, the minimum grid discretization seems to be related to the minimum curvature value of the wave. Both damped and undamped wave surface topographies with different curvature values are studied to obtain fairly accurate results. This makes the method viable for experimental validation, which is being investigated in an ongoing work. The method seemed to work equally well for waves with larger curvatures with the optimum values of parameters.

ACKNOWLEDGMENTS

We acknowledge the support from the Ministry of Education and Research of Norway (Grant No. 8050 IN-12593). We thank Professor Hans Joakim Skadsem for his support and colleagues from the Multiphase Flow Lab at University of Stavanger, Norway, for their suggestions and encouragement.

AUTHOR DECLARATIONS

Conflict of Interest

The authors have no conflicts to disclose.

Author Contributions

V. V. Mukim: Conceptualization (equal); Formal analysis (equal); Methodology (equal); Writing – original draft (equal); Writing – review & editing (equal). **R. W. Time**: Conceptualization (equal); Funding acquisition (equal); Supervision (equal); Writing – review & editing (equal). **U. R. Kanade**: Formal analysis (equal); Writing – review & editing (equal). **A. H. Rabenjafimanantsoa**: Conceptualization (equal); Funding acquisition (equal); Supervision (equal); Writing – review & editing (equal).

DATA AVAILABILITY

The data that support the findings of this study are available from the corresponding author upon reasonable request.

REFERENCES

[1]W. Munk, "Origin and generation of waves," in *Proceedings 1st International Conference on Coastal Engineering* (American Society of Civil Engineers, **1950**), pp. 1–4.
[2]F. Behroozi, J. Smith, and W. Even, "Stokes' dream: Measurement of fluid viscosity from the attenuation of capillary waves," Am. J. Phys. **78**, 1165–1169 (2010).
[3]J. Lighthill, *Waves in Fluids* (Cambridge University Press, 1978), Chaps. 3.1–3.5, pp. 204–237.
[4]F. Behroozi and N. Podolefsky, "Dispersion of capillary-gravity waves: A derivation based on conservation of energy," Eur. J. Phys. **22**, 225 (2001).
[5]R. I. Slavchov, B. Peychev, and A. S. Ismail, "Characterization of capillary waves: A review and a new optical method," Phys. Fluids **33**, 101303 (2021).
[6]T. K. Barik, A. Roy, and S. Kar, "A simple experiment on diffraction of light by interfering liquid surface waves," Am. J. Phys. **73**, 725–729 (2005).
[7]T. K. Barik, P. R. Chaudhuri, A. Roy, and S. Kar, "Probing liquid surface waves, liquid properties and liquid films with light diffraction," Meas. Sci. Technol. **17**, 1553 (2006).
[8]F. Zhu, R. Miao, C. Xu, and Z. Cao, "Measurement of the dispersion relation of capillary waves by laser diffraction," Am. J. Phys. **75**, 896–898 (2007).
[9]D. Nikolić and L. Nešić, "Determination of surface tension coefficient of liquids by diffraction of light on capillary waves," Eur. J. Phys. **33**, 1677 (2012).
[10]D. Chowdhury, S. Bhunia, and T. K. Barik, "Study the liquid surface capillary wave profile by optical method," Int. J. Soft Comput. Eng. **2**(6), 386–390 (2013).
[11]J. R. Saylor, "Internal reflection beneath capillary water waves: A method for measuring wave slope," Appl. Opt. **36**, 1121–1129 (1997).
[12]C. S. Palm, R. C. Anderson, and A. M. Reece, "Laser probe for measuring 2-D wave slope spectra of ocean capillary waves," Appl. Opt. **16**, 1074–1081 (1977).
[13]J. R. Saylor and R. A. Handler, "Gas transport across an air/water interface populated with capillary waves," Phys. Fluids **9**, 2529–2541 (1997).
[14]F. Behroozi, B. Lambert, and B. Buhrow, "Noninvasive measurement of viscosity from damping of capillary waves," ISA Trans. **42**, 3–8 (2003).
[15]F. Behroozi and A. Perkins, "Direct measurement of the dispersion relation of capillary waves by laser interferometry," Am. J. Phys. **74**, 957–961 (2006).
[16]M. Wei, S. Huang, J. Wang, H. Li, H. Yang, and S. Wang, "The study of liquid surface waves with a smartphone camera and an image recognition algorithm," Eur. J. Phys. **36**, 065026 (2015).
[17]X. Zhang, "Capillary–gravity and capillary waves generated in a wind wave tank: Observations and theories," J. Fluid Mech. **289**, 51–82 (1995).
[18]F. Moisy, M. Rabaud, and K. Salsac, "A synthetic Schlieren method for the measurement of the topography of a liquid interface," Exp. Fluids **46**, 1021–1036 (2009).
[19]H.-C. Liu, P. Kijanka, and M. W. Urban, "Fluid surface tension evaluation using capillary wave measurement with optical coherence tomography," AIP Adv. **10**, 055121 (2020).
[20]X. Shao, C. Gabbard, J. Bostwick, and J. Saylor, "On the role of meniscus geometry in capillary wave generation," Exp. Fluids **62**, 1–4 (2021).
[21]E. Hecht, Optics, 4th ed. (Addison-Wesley, 2001), Chaps. **4**.4–4.5, pp. 100–111.